# Silicon carbide with tunable ordered mesoporosity

Peng-Cheng Gao, Patrice Simon, Frédéric Favier

# Silicon carbide with tunable ordered mesoporosity

Peng-Cheng Gao [a,c], Patrice Simon [b,c], Frédéric Favier [a,c,*]

[a] Institut Charles Gerhardt Montpellier UMR 5253 CNRS, Université Montpellier 2, cc1502, 34095 Montpellier cedex 05, France
[b] Université Paul Sabatier, CIRIMAT UMR CNRS 5085, 118 route de Narbonne, 31062 Toulouse, France
[c] Réseau sur le Stockage Electrochimique de l'Energie (RS2E), FR CNRS 3459, France

A B S T R A C T

Tunable mesoporous silicon carbides (SiCs) are synthesized by magnesio-thermal reduction of homogeneous composites of silica and carbon precursors. Two triblock copolymers, P123 and F127, are used as structuring agents leading to composites showing an hexagonal mesoporous pattern which is kept by the final SiC thanks to the relatively low temperature of the magnesio-thermal reduction. Two series of mesoporous SiCs are obtained with uniform pore sizes ranging from 6.0 nm to 2.5 nm (P123 used as structuring agent) and 11.0–3.5 nm (F127) depending on the carbon/silica molar ratio in the pristine composite. In each series, SiC polytype transforms from 6H–SiC to 3C–SiC in pace of increasing the carbon content in the composite precursor. A multi step growth mechanism is proposed to account for the composite precursor to final carbide characteristics.

*Keywords:*
Mesoporous silicon carbide
Magnesio-thermal reduction
SiC polytype
Tunable ordered structure
Growth mechanism

## 1. Introduction

Mesoporous silicon carbide (SiC), thanks to its high hardness, temperature stability and flourish porosity [1], is a valuable material for abrasives or refractories of precise devices such as steam stable membranes [2], porous burners [3], solar absorbers [4] and catalysis supports [5]. Ordered Mesoporous Silicon Carbides (OMSC) overpass ordered mesoporous carbon analogues in most of the application areas but inherit their synthetic routes. OMSC was firstly synthesized by hard template casting using polysiloxanes [6] and polycarbosiloxanes [7,8] as common precursors. After impregnation and template removal, the siloxane precursor was thermally converted to silicon carbide. By using SBA-15 silica template, the surface area of the resulting OMSC reached up to 508 $m^2$/g [9]. There are also several reports about direct carbothermal reduction of the silica template by the impregnated carbon. Resulting mesopororous SiC typically showed a 150 $m^2$/g surface area and pore sizes ranging from 2 to 4 nm [10]. A recent US patent stated on the synthesis of porous SiC by carbothermal reduction through a soft template approach using a nonionic surfactant polyol as structuring agent [11]. The final product developed a surface area of 876 $m^2$/g and pore sizes ranging from 4 to 5 nm. However, above carboreduction strategies require high conversion temperatures ranging from 1400 to 2000 °C. Beside the risks of porous structure collapsing and material sintering, the operating cost multiplies with the need of high temperature furnaces as well as high purity inert gas. Shi et al. recently demonstrated the efficiency of magnesium in lowering the temperature of synthesis of SiC down to 700 °C [12]. In the same time-frame, we introduced SBA-15 and 3D Stöber matrix as hard template and successfully synthesized meso and macroporous SiCs using a similar magnesio-thermal reduction at 800 °C [13]. During the process, reduced silicon oxide ($SiO_x$) diffuses into carbon, unfortunately causing a partial collapsing of the original framework and a loss of the ordered arrangement of the pristine template. To limit this detrimental diffusion, a porous carbon–silica composite framework can be considered. On the other hand, in the course of ordered mesoporous silica or carbon from carbon–silica composites through a soft template approach, the pore size of the composite was shown to be controllable by altering the ratio between the silica and the carbon precursors [14]. This soft-template approach seems to offer a carbon–silica framework suited for the magnesio-thermal synthesis of OMSCs with tunable porous characteristics.

On the other hand, SiC exhibits a unique polymorphism with over 250 polymorphs identified [15,16]. Polytypes of SiCs are mostly cubic (C) or hexagonal (H) and originate from the identical variations of C or Si terminating layer in two or three dimensions [16,17]. Depending on the preparation route (CVD, LPE deposition, VLS growth…) [18] and synthetic parameters (temperature [19], alkaline dopants [20], Si/C ratio [21], graphitization [22], metal additives [23]…) 3C-, 4H-, 6H-…SiCs are obtained.

Herein, we report a novel synthetic route for OMSCs with controllable pore sizes prepared by magnesio-thermal reduction of

* Corresponding author at: Institut Charles Gerhardt Montpellier UMR 5253 CNRS, Université Montpellier 2, cc1502, 34095 Montpellier cedex 05, France. Tel.: +33 (0) 4 67 14 33 32; fax: +33 (0) 4 67 14 33 04.
*E-mail address:* fredf@univ-montp2.fr (F. Favier).

http://dx.doi.org/10.1016/j.micromeso.2013.06.027

soft templated carbon–silica composite precursors. Both Pluronic® F-127 and Pluronic® P-123 serve as surfactant agents to synthesize ordered polymer/silica composites. With the help of Mg, the complete reduction of the carbon–silica precursor to silicon carbide is achieved at 800 °C. The final silicon carbide well inherits the ordered arrangement from its carbon–silica precursor. Thanks to this moderate synthetic temperature and since any carbon is consumed by carboreduction, dense SiC walls are obtained preventing the porous structure to shrink or collapse. The effect of the carbon/silica molar ratio on the pore size of the resulting SiC is explored through TEM, SAXS and $N_2$-adsorption characterizations. In addition, the observed transition from 6H-SiC to 3C–SiC polytype, depending on the synthetic parameters, is explained by XRD and IR analyses. A growth mechanism of mesoroporous SiC by the presented method is proposed.

## 2. Experimental

### 2.1. Synthesis of ordered mesoporous carbon/$SiO_2$ precursor

Mesoporous carbon–silica composites were prepared with slight modifications on the synthetic route described by Liu et al. [14]. In the following example, triblock copolymer P123 (Aldrich) was chosen as soft template. In a typical procedure, under vigorous stirring, 1.0 g of 0.2 M HCl was added to 9.6 g of 20 wt.% P123 alcoholic solutions. After stirring at 40 °C for 4 h, a clear solution is obtained. Subsequently, 1 g of 20 wt.% resol alcoholic solution (refer to SI for details) and 2.08 g tetraethoxysilane (TEOS, 98% Alfa Aesor) were added. In this series, the amount of silica precursor (TEOS) was kept at 2.08 g, meanwhile the amount of carbon precursor (resol alcoholic solution, the Resin hereafter) was increased from 1 g up to 5 g to vary the carbon/silica ratio. The mixture was continuously stirred for 2 h and painted afterwards onto a glass plate. The resulting film was kept at ambient temperature overnight to evaporate residual ethanol before being polymerized at 100 °C for 24 h. The as-made film was scraped and ground into fine powder before being heated in a tubular furnace at 800 °C for 3 h under $N_2$ flow. At this step, Resin and Pluronic® are being carbonised, and hydroxyl groups from TEOS hydrolysis condensed to form the C/$SiO_2$ composite. C/Si molar ratio were calculated by left silica content after burning SiC precursors in air at 550 °C for 2 h.

### 2.2. 2. Magnesio-thermal treatment of the precursors

Mesoporous silicon carbide was synthesized by using Mg as reducing agent at moderate temperature as described in our recent work [13]. Briefly, in a glove box filled with Ar, carbon/$SiO_2$ composite powder and Mg grids were mixed uniformly by manual grinding. Mg owned a 10% molar excess over $SiO_2$ content (Mg/$SiO_2$ = 2.2). The fine powder was then sealed under Ar in a 316L stainless tube. The magnesio-thermal treatment was processed at 800 °C for 24 h at a heating rate of 1 °C/min. The excess of Mg was gently hydrolized in air before the final product to be purified using 1 M HCl and 1 M $HNO_3$ aqueous solution in sequence.

In the rest of the text, powder samples at various synthetic stages are named as XX–Y–zz. XX refer to the carbon–silica composite (CS) or silicon carbide (SiC), Y can be either P or F depending on the surfactant used for soft templating, i.e., P123 or F127. zz refers to the C/$SiO_2$ molar ratios after carbonization. For example, the sample named by CS-P-47 is a carbon–silica composite powder with a C/$SiO_2$ ratio at 0.47 prepared by using P123 as surfactant. After magnesio-thermal reduction, the corresponding silicon carbide powder is named by SiC-P-47 accordingly while SiC-F-162 refers to a SiC sample prepared by using F127 surfactant and a C/$SiO_2$ ratio after carbonisation at 1.62. Synthetic conditions are listed in Table 1 for the whole series of prepared powders.

**Table 1**
Preparation condition and composite compositions of the C/$SiO_2$ composites after carbonization.

| | TEOS (g) | Resol (g) | P123 or F127 (g) | C/$SiO_2$ ratio[a] |
|---|---|---|---|---|
| SiC-P-47 | 2.08 | 1.0 | 1.6 | 0.47 |
| SiC-P-81 | 2.08 | 2.0 | 1.6 | 0.81 |
| SiC-P-103 | 2.08 | 2.5 | 1.6 | 1.03 |
| SiC-P-121 | 2.08 | 3.0 | 1.6 | 1.21 |
| SiC-P-134 | 2.08 | 4.0 | 1.6 | 1.34 |
| SiC-P-153 | 2.08 | 5.0 | 1.6 | 1.53 |
| SiC-F-86 | 2.08 | 1.0 | 1.6 | 0.86 |
| SiC-F-104 | 2.08 | 2.0 | 1.6 | 1.04 |
| SiC-F-130 | 2.08 | 3.0 | 1.6 | 1.30 |
| SiC-F-162 | 2.08 | 4.0 | 1.6 | 1.62 |
| SiC-F-214 | 2.08 | 5.0 | 1.6 | 2.14 |

[a] The mass percentage in carbon–silica composites, determined by weighing after burning carbon at 550 °C.

### 2.3. Characterization and measurements

X-ray diffraction (XRD) and small-angle X-ray scattering (SAXS) measurements were performed on a Phillips X′ Pert diffractometer using Cu Kα radiation ($\lambda$ = 1.5405 Å). Scanning Electron Micrographs (SEM) and Transmission Electron Microscope pictures (TEM) were taken using a JEOL JSM-6300F SEM microscope and a JEOL 1200 EX2 TEM microscope operating at 100 kV, respectively.

Porous characteristics were calculated from nitrogen sorption isotherms measured at 77 K with a Micromeritics ASAP 2020 equipment. The specific surface area was estimated by using Brunauer–Emmett–Teller (BET) method while the pore volumes and the pore size distributions were calculated by using Barrett–Joyner–Halenda (BJH) method from adsorption isotherms [24]. Fourier Transformed Infrared (FT-IR) spectra of samples were recorded with ART objective by using a Labram ARAMIS IR2 spectrometer from Horiba-Jobin Yvon.

## 3. Results and discussion

Fig. 1 shows the XRD patterns of the final SiCs deriving from carbon–silica composites with incremental carbon contents. For all samples, three main diffraction peaks appear at about 35.6°, 60.0° and 71.8° (2$\theta$), corresponding to the (111), (220) and (311) diffraction peaks of cubic *F*-43 m SiCs. It suggests the surfactant nature, P or F, not to impact on the structural arrangement and to lead to a cubic SiC lattice. However, in Fig. 1(A), SiC-P-81 displays narrow extra peaks at 33.6°, 38.1°, 71.7° and 75.4° (2$\theta$), corresponding, respectively to (100), (101), (112) and (004) diffractions of hexagonal 6H-SiC. This community of cubic- and hexagonal- crystallites relates to the polytypism of SiC. As the carbon content increases, the intensities of the hexagonal peaks, (100) and (101), are fading down as shown from SiC-P-47 (Fig. 1A-a) to SiC-P-103 (Fig. 1A-c) patterns. For SiC-P-121 (Fig. 1A-d) and samples from higher C/$SiO_2$ ratio, patterns are characteristic of a 3C–SiC structure without any hexagonal features. SiC-P-153 (Fig. 1A-f) owns a wide diffraction peak in the 20° to 30° (2$\theta$) range assigned to amorphous carbon originating from the excess carbon in its composite precursor.

$$SiO_2/C + 2Mg - 800^{\circ}C/Ar \rightarrow SiO_x(v) + C(s) + (2-x)MgO(s) + xMg(l) \rightarrow SiC + 2MgO \quad (1)$$

In the presented synthetic route, heating at 800 °C under sealed conditions allows the reactant mixture to come into a complex vapor–liquid–solid system composed of $SiO_x$ vapors, Mg melts and

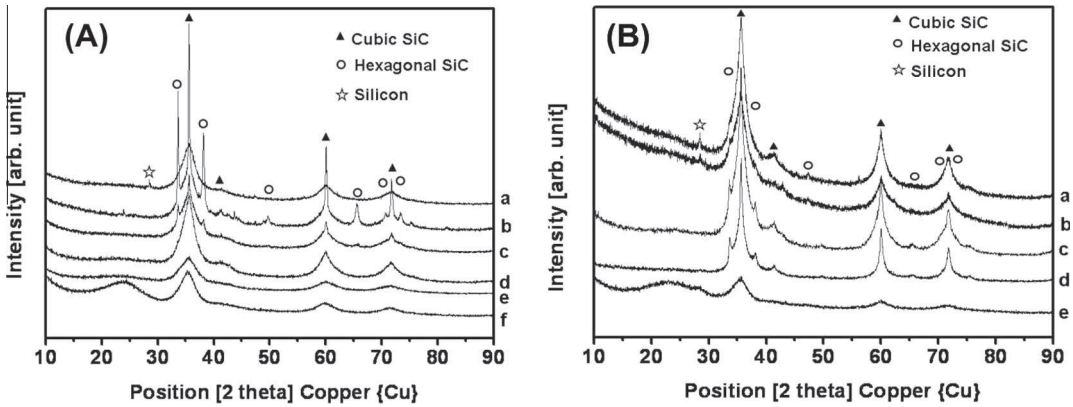


**Fig. 1.** XRD patterns of SiC P-series (A) and SiC F-series(B). In (A), a, b, c, d, e and f correspond to SiC-P-47, SiC-P-81, SiC-P-103, SiC-P-121, SiC-P-134 and SiC-P-153, respectively. In (B), a, b, c, d and e correspond to SiC-F-86, SiC-F-104, SiC-F-130, SiC-F-162 and SiC-F-214, respectively.

carbon crucible (Eq. (1)) [13]. Mg owns a typical hexagonal crystal structure at solid state [25]. During the reduction, melting Mg incorporates inside the nucleating SiC lattice and promotes the growth of hexagonal SiC [17]. As such, 6H-SiC appears, especially when the carbon/silica ratio is equal to or less than 1. In contrast, in carbon–silica composites with high carbon content, the excess of graphitized carbon favors the nucleation of 3C–SiC lattices [22]. Hence, the hexagonality of SiCs weakens along with increasing the carbon content in the reaction medium. Fig. 1(B) shows the XRD patterns of SiC F-series. When the $C/SiO_2$ ratio is close to or less than 1, SiC owns the cubic SiC diffractions with traces of silicon impurities.

The lattice of SiC-F-130 (Fig. 1B-c) and SiC-F-162 (Fig. 1B-d) presents the features of the 6H-form together with those of the 3C–SiC. In the SiC F-series, by increasing the carbon content, resulting SiCs show a variation of crystal structure similar to P-series. Whereas, for generating the 6H-SiC form, the carbon consumption in the F-series is higher than in the P-series. SiC-F-214 pattern (Fig. 1B-e) also shows the amorphous carbon peak between 20° and 30° ($2\theta$). In both P and F series, final SiCs show a diversification from 6H-SiC to 3C–SiC polytypes by altering the $C/SiO_2$ ratio in their precursor: the higher the ratio, the lower the hexagonal character. Infrared spectra (IR) (Fig. S1 (A) and (B)) do not show any obvious adsorption peak of $SiO_2$ or carbon neither in P- nor F-series of prepared SiCs and confirm the complete conversion of the pristine carbon–silica composite. In the whole series, adsorption bands appear at about 1040 $cm^{-1}$ and are assigned to $Si–CH_2–Si$ stretching. The sharpness of the disilymethylene band helps to distinguish

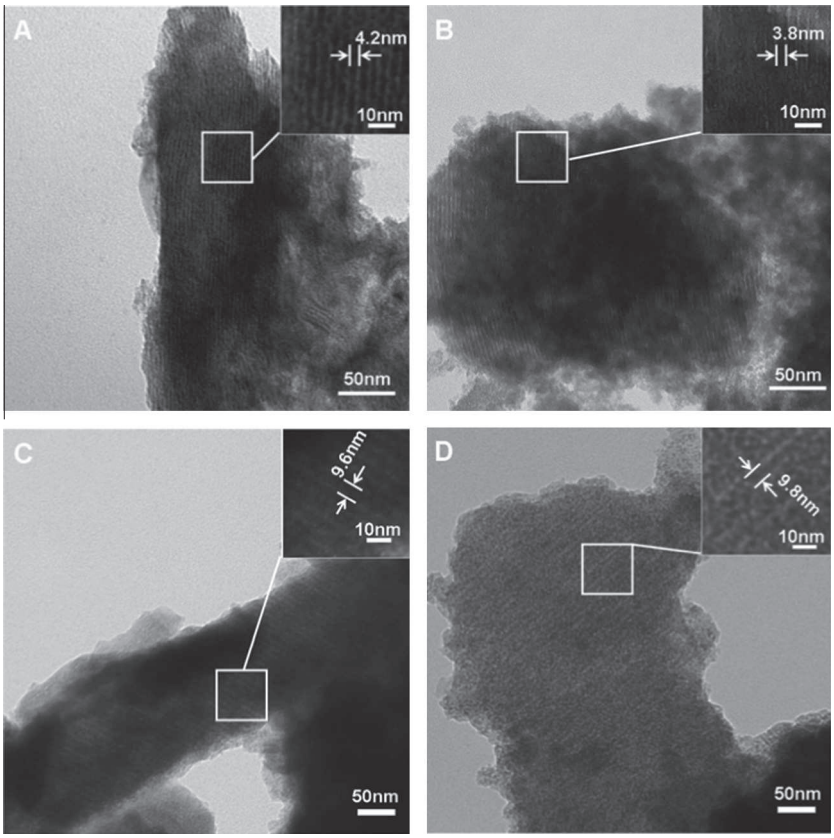


**Fig. 2.** TEM images of mesoporous silicon carbide,SiC-P-103 and SiC-P-134 (A and B, respectively), SiC-F-104 and SiC-F-130 (C and D, respectively).

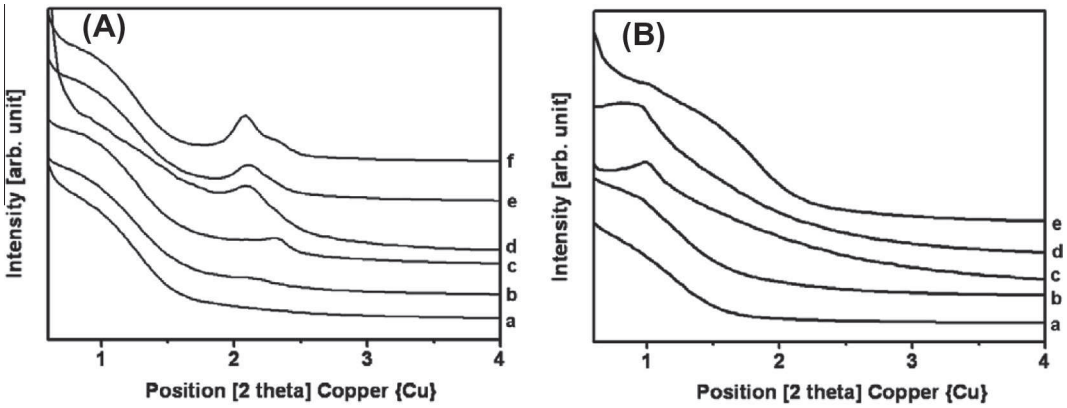


**Fig. 3.** SAXS patterns a of SiC P-series (A) and SiC F-series (B). In (A), a, b, c, d, e and f correspond to SiC-P-47, SiC-P-81, SiC-P-103, SiC-P-121, SiC-P-134 and SiC-P-153, respectively. In (B), a, b, c, d and e correspond to SiC-F-86, SiC-F-104, SiC-F-130, SiC-F-62 and SiC-F-214, respectively.

**Table 2**
Physicochemical Properties of the mesoporous silicon carbide with different $C/SiO_2$ molar ratio.

| | $D$ (nm) | $A_0$ (nm) | $S_{BET}$ ($m^2/g$) | $V$ ($cm^3/g$) |
|---|---|---|---|---|
| SiC-P-47 | 6.0/50 | – | 333 | 0.34 |
| SiC-P-81 | 3.7 | 4.2 | 413 | 0.36 |
| CS-P-103 | – | – | 3.0 | 0.01 |
| SiC-P-103 | 3.5 | 4.1 | 497 | 0.63 |
| CS-P-121 | – | – | 6.1 | 0.02 |
| SiC-P-121 | 3.1 | 3.8 | 519 | 0.52 |
| SiC-P-134 | 2.7 | 4.2 | 559 | 0.46 |
| SiC-P-153 | 2.5 | 4.3 | 634 | 0.44 |
| CS-F-86 | 5.1 | – | 291 | 0.45 |
| SiC-F-86 | 11 | – | 245 | 0.27 |
| CS-F-104 | 5.4 | – | 330 | 0.50 |
| SiC-F-104 | 5.3 | 9.0 | 421 | 0.49 |
| CS-F-130 | 4.0 | – | 273 | 0.33 |
| SiC-F-130 | 4.6 | 9.2 | 629 | 0.78 |
| CS-F-162 | 3.7 | – | 362 | 0.39 |
| SiC-F-162 | 4.0 | 9.3 | 741 | 0.69 |
| CS-F-214 | 3.3 | – | 183 | 0.20 |
| SiC-F-214 | 3.5 | 9.1 | 643 | 0.52 |

$D$ is the pore size diameter. $A_0$ is the interlayer distance measured by SAXS. $S_{BET}$ is the BET surface area. $V$ is the total pore volume.

it from Si–O–Si stretching bands in the same wavelength range [26]. In Fig. S1 (C), all P-series samples show the characteristic absorption bands of SiCs, originating from optical Fuchs–Kliewer surface phonons, at about 924 $cm^{-1}$ (Longitudinal Optical (LO) modes) [27]. In the range from 750 to 800 $cm^{-1}$ (corresponding to transverse optical (TO) phonon), the singlet of SiC-P-47 at 770 $cm^{-1}$ is assigned to 8H-SiC or 10H-SiC allotropes which both own a higher hexagonality than 6H-SiC. The IR spectrum of SiC-P-81 shows two bands at 784 $cm^{-1}$ (TO modes in the SiC basal lattice plane) and 757 $cm^{-1}$ (TO modes parallel to the main axes). This doublet is characteristic of the 6H-SiC structure. However, the sub-equal intensities indicate the coexistence of 6H-SiC together with SiC with higher hexagonality. By increasing the carbon content in precursor, the intensity of the shoulder peak at about 757 $cm^{-1}$ decreases. Furthermore, the shift of the main band from 784 $cm^{-1}$ for SiC-P-81 to 794 $cm^{-1}$ for SiC-P-134 clearly points out the progressive predominance of the 3C–SiC polytype in SiC-P-134. SiC-P-153 owns a singlet at 792 $cm^{-1}$ fitting the expected value for basal TO modes in 3C–SiC at 795 $cm^{-1}$. In Fig. S1 (D), all SiC samples of the F-series also show characteristic absorption bands at about 924 $cm^{-1}$. Increasing the carbon content induces a shift of the bands of the SiC F-series from 775 $cm^{-1}$ to 810 $cm^{-1}$ which fits the observed trend in P-series bands. Together with the XRD results, it can be concluded from IR analysis that a larger carbon content in the precursor decreases the hexagonality of the final SiC.

TEM images of prepared SiCs in Fig. 2 show well-proportioned fringes in both P- and F- series samples characteristic of ordered 2-D arrays. These micrographies confirm that, through Mg reduction, SiCs well inherit the ordered matrix from the pristine $C/SiO_2$ units without any structure shrinkage or collapsing.

The interlayer distance in SiC-P series remains roughly the same with $4.2 > D > 3.8$ nm, independently from the initial carbon/silica content. SAXS reflections shown in Fig. 3 (A) further confirm the highly ordered structures of prepared carbides with distances consistent with those measured by TEM. Compared to the P-series, F-series carbides obviously own larger interlayer distances: SiC-F-130 and SiC-F-162 also present an ordered 2-D arrangement of pores with 9.6 nm and 9.8 nm interlayer distance, respectively, as measured from Fig. 2(C) and (D). This almost constant $A_0$ distance is confirmed at about 9.2 nm in SAXS patterns from Fig. 3 (B). $A_0$ distances are collected in Table 2 for both series. The larger parameter of F-series carbide stems from the longer triblock chain of F127 than P123. With carbon/silica ratio below 1, the SiC ordering is lost as demonstrated by the absence of SAXS peaks. At these ratio, there is too much $SiO_x$ generated during the magnesio-thermal treatment, and after reduction the walls of the porous structure are composed of a mixture of SiC, Si and unreduced silica. After Si and silica removal by acidic treatments, only SiC parts are left ending up with a collapsing of the whole structure because of the breakdown of the walls resulting in a loss of the pristine ordering. With $C/SiO_2$ above or equal to 1, the ordering is kept.

In Fig. 4(A), $N_2$ sorption isotherms of SiC P-series usually exhibit type-I curves and H4-type hysteresis loop which are typical of mesoporous materials. The strong adsorption in the $P/P_0 = 0–0.1$ low pressure range indicates the presence of micropores too. SiC-P-47 owns a type-II curves with a sharp capillary condensation step at $P/P_0 = 0.9–1.0$ and H3-type hysteresis. As listed in Table 2, the specific BET surface areas of the P-series SiCs are ranging from 333 $m^2/g$ to 634 $m^2/g$ and increase with the carbon content in the precursor. In contrast, the pore volumes are randomly ranging from 0.34 $cm^3/g$ (SiC-P-47) to 0.63 $cm^3/g$ (SiC-P-103). The highest porous volume is obtained from a $C/SiO_2$ ratio close to 1. All P-series silicon carbides but SiC-P-47 own narrow distributions of pore sizes as shown in Fig. 4(C). With increasing the carbon content in the precursor, pore size decreases from 3.7 nm to 2.5 nm from SiC-P-81 to P-153. The large and broadly distributed pores of SiC-P-47 mainly comes from disordered particle stacking. The same trend is observed in the F series. $N_2$ sorption isotherms (Fig. 4(B)) of SiC-F-162 and SiC-F-214 are type-I curves and H4-type hystere-

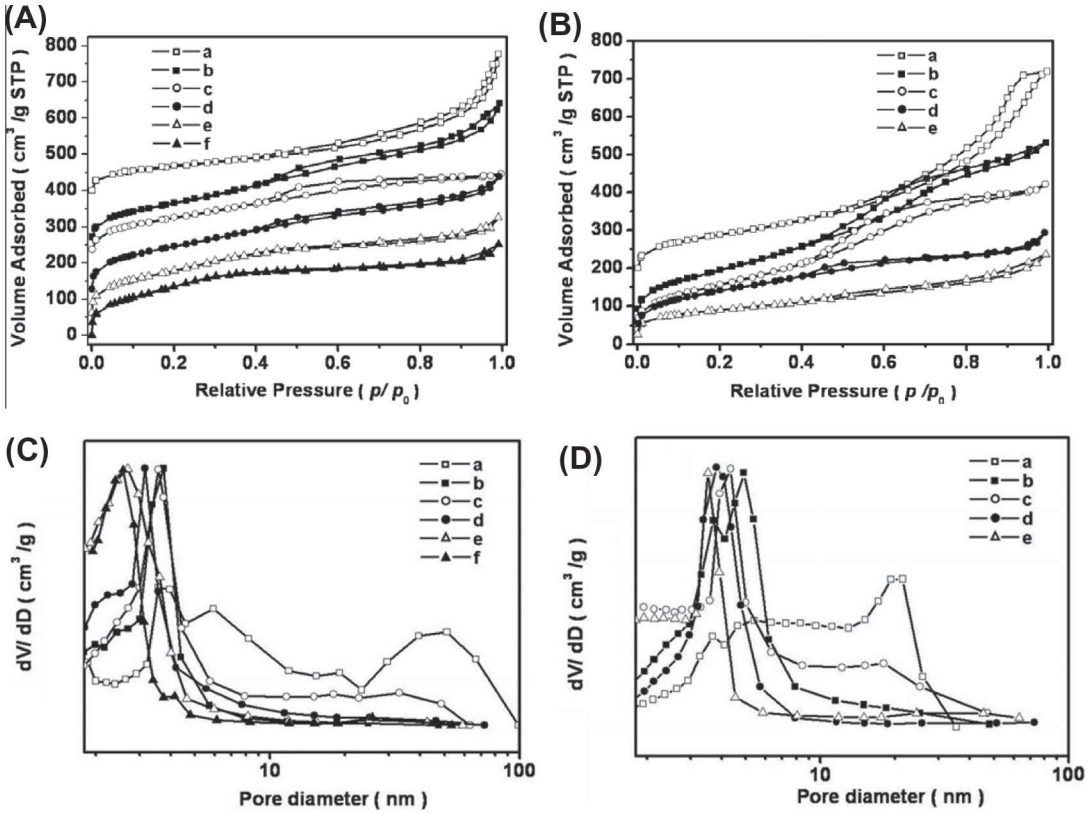


**Fig. 4.** $N_2$ sorption isotherms curves and pore size distributions of P-series SiCs (A and C) and F-series SiCs (B and D). In A and C, a, b, c, d, e and f correspond to SiC-P-47, SiC-P-81, SiC-P-103, SiC-P-121, SiC-P-134 and SiC-P-153, respectively. In B and D, a, b, c, d and e correspond to SiC-F-86, SiC-F-104, SiC-F-130, SiC-F-162 and SiC-F-214, respectively.

sis loops. SiC-F-104 and SiC-F-130, deriving from composites of lower carbon content, own a type-II curves and H2-type hysteresis loops. The mild capillary condensation step at $P/P_0 = 0.5–0.8$ is characteristic of the material mesoporosity. The sorption isotherm of SiC-F-86 presents a type-III isotherm and H3-type hysteresis loop which is consistent with the large pores formed by the flake

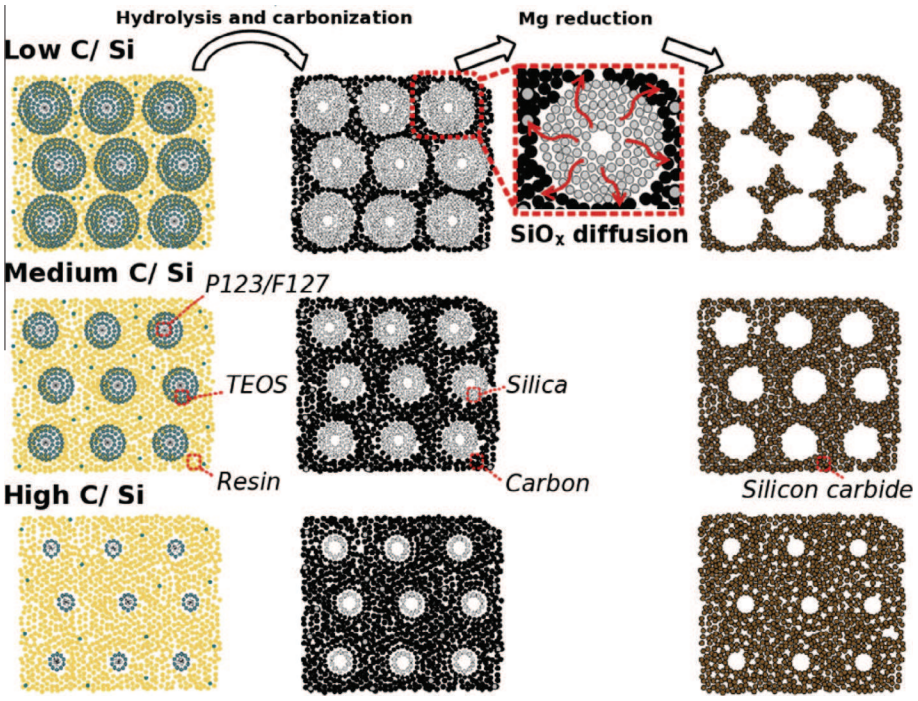


**Fig. 5.** SiC growth mechanism starting form various CS composite precursors. The pore size of the final SiC depends on the liquid polymer/TEOS ratio thanks to the size of the silica shell around the P123/F127 micelles. During the magnesio-thermal reduction, $SiO_2$ dissolves through $SiO_x$ diffusion through the carbon matrix for pore opening in the final SiCs.

particle stacks. In the F-series, pores range from 11 to 3.5 nm as the $C/SiO_2$ ratio increases from SiC-F-86 to SiC-F-214.

To complete the SiC structure description, the wall thicknesses can be extracted from interplanar distances and pore diameters, respectively $A_0$ and $D$ as listed in Table 2. In both SiC series, along with the pore size decrease, the wall thicknesses increase from 0.5 nm to 1.8 nm in the P-series and from 3.7 nm to 5.6 nm in the F-series.

In the P series, CS-P carbon–silica precursors obtained by carbonization at 800 °C do not show any BET surface nor porous volume (or very limited for CS-P-103 and CS-P-121) and the porosity is opened during the SiC formation through magnesio-thermal reaction. In contrast, CS-F composites are porous and pore sizes, although smaller than in the final corresponding SiCs, roughly follow the same evolution: the higher the $C/SiO_2$ ratio the smaller the pore size. This point confirms the porous characteristics of the prepared SiCs to originate from those of the corresponding CSs and allows to suggest a coherent SiC formation mechanism. Fig. 5 summarizes the suggested mechanism and, accordingly, the impact of the $C/SiO_2$ content in the composite precursor on the SiC final porous structure: CS composites are structured through the interactions between P123 or F127 polar parts and TEOS hydrophilic parts. As such, the direct surrounding of the structuring agent micelles is TEOS rich. By hydrolysis, a silica-rich shell is formed around the P or F polymer core. During the polymerization and carbonization, triblock copolymer P123 and F127 limit the unit parameter at about 4.2 nm and 9.2 nm, respectively. In a single carbon–silica composite unit, the occupied volume of carbon enlarge along with the increase of the carbon content. Correspondingly, the volume of silica shrinks because of the limited space per unit. As such, both silica shell and CS composite wall thicknesses depend on the $C/SiO_2$ ratio: thin silica shell and thick C-rich walls for high $C/SiO_2$ ratio and vice and versa. In our previous work, we used 3D stöber silica matrix as template impregnated by furfuryl alcohol [13]. After magnesio-thermal reduction, the macroporous SiC matrix emerged. The inverted duplicate from silica stöber ball to macroporous SiC matrix unambiguously suggests the diffusion from silica to carbon during the magnesio-thermal reduction and not the other way around. Similarly, in the present case, $SiO_x$ vapors generated during the magnesio-thermal reaction actually diffuse through the composite, inducing a dissolution of the silica shell and an increase in the resulting pore diameter from CS composites to final SiCs, as observed in Table 2. The larger the $C/SiO_2$ ratio, the thicker the silica shell in the composite and the larger the pore diameter/the thinner the wall thickness in the corresponding SiC. The wide and irregular distributions in SiC-P-47 and SiC-F-86 are mainly caused by the perforation of pores during the magnesio-thermal reduction and wall collapsing.

## 4. Conclusion

Tunable mesoporous silicon carbides were synthesized by magnesio-thermal reduction of carbon–silica composites with different molar ratios. It should be emphasized that the evidence presented in the paper is mainly XRD and IR, which indicates that the SiC polytypes in Mg-doping VLS system were revealed to alter from 6H-SiC to 3C–SiC along with the increasing carbon/silica molar ratio. With the incremental carbon/silica ratio in precursor, the pore sizes of SiCs present downtrend correspondingly. The narrow distributions of final SiCs span from 2.5 nm to 3.7 nm and from 3.5 nm to 5.3 nm in the two SiC series using P123 and F127 as structuring agent, respectively. P123 and F127 limit the unit parameter of SiC as 4.2 nm and 9.2 nm, respectively. The wall thickness of SiC increases along with the decreasing pore sizes. Finally, the suggested mechanism of SiC growth is based on the diffusion of $SiO_x$ from $SiO_2$ rich micelle surroundings to carbon rich matrix during the magnesio-thermal reaction in accordance with the observed porosity characteristics.


## Acknowledgments

The authors acknowledge the CNRS funding. PCG would like to thank the Chinese Scientific Council for fellowship.


## Appendix A. Supplementary data

Supplementary data associated with this article can be found, in the online version, at http://dx.doi.org/10.1016/j.micromeso.2013.06.027.

## References


[1] L. Borchardt, C. Hoffmann, M. Oschatz, L. Mammitzsch, U. Petasch, M. Herrmann, S. Kaskel, Chem. Soc. Rev. 41 (2012) 5053–5064.
[2] M. Fukushima, Y. Zhou, H. Miyazaki, Y. Yoshizawa, K. Hirao, J. Am. Ceram. Soc. 89 (2006) 1523–1529.
[3] U.F. Vogt, L. Györfy, A. Herzog, T. Graule, G.J. Plesch, Phys. Chem. Solids 68 (2007) 1234–1238.
[4] C.C. Agrafiotis, I. Mavroidis, A.G. Konstandopoulos, B. Hoffschmidt, P. Stobbe, M. Romero, V. Fernandez-Quero, Sol. Energy Mater. Sol. Cells 92 (2007) 474–481.
[5] M.J. Ledoux, C. Crouzet, P. Cuong, V. Turines, K. Kourtakis, P.L. Mills, J.J. Lerou, J. Catal. 203 (2001) 495–508.
[6] J.H. Eom, Y.W. Kim, I.H. Song, H.D. Kim, J. Eur. Ceram. Soc. 28 (2008) 1029–1035.
[7] Y. Shi, Y. Meng, D. Chen, S. Cheng, P. Chen, H. Yang, Y. Wan, D. Zhao, Adv. Funct. Mater. 16 (2006) 561–567.
[8] P. Krawiec, D. Geiger, S. Kaskel, Chem. Commun. 23 (2006) 2469–2470.
[9] P. Krawiec, C. Weidenthaler, S. Kaskel, Chem. Mater. 16 (2004) 2869–2880.
[10] A.H. Lu, W. Schmidt, W. Kiefer, F. Schüth, J. Mater. Sci. Lett. 40 (2005) 5091–5093.
[11] S.B. Dawes, W. Senaratne, Synthesis of ordered mesoporous carbon–silicon nanocomposites. US. Patent 12, 190, 867, august 13, 2008.
[12] Y. Shi, F. Zhang, Y.S. Hu, X.H. Sun, Y. Zhang, H.L. Lee, L. Chen, G.D. Stucky, J. Am. Chem. Soc. 132 (2010) 5552–5553.
[13] P.C. Gao, Y. Lei, A.C. Pérez, K. Rajoua, D. Zitoun, F. Favier, J. Mater. Chem. 21 (2011) 15798–15805.
[14] R. Liu, Y. Shi, Y. Wan, Y. Meng, F. Zhang, D. Gu, Z. Chen, B. Tu, D. Zhao, J. Am. Chem. Soc. 128 (2006) 11652–11662.
[15] Y.M. Tairov, V.F. Tsvetkov, J. Cryst. Growth 52 (1981) 146–150.
[16] B. Wenzien, P. Käckell, F. Bechstedt, Phys. Rev. B 52 (1995) 10897–10905.
[17] A.R. Verma, P. Krishna, Polymorphism and Polytypism in Crystals, Wiley, New York, 1966.
[18] G. Ferro, C. Jacquier, New J. Chem. 28 (2004) 889–896.
[19] A. Zywietz, K. Karch, F. Bechstedt, Phys. Rev. B 54 (1996) 1791–1798.
[20] S.A. Sakwe, R. Müller, P.J. Wellmann, J. Cryst. Growth 289 (2006) 520–526.
[21] A. Fiessel, Phys. Rep. 379 (2003) 149–255.
[22] M. Soueidan, G. Ferro, Adv. Funct. Mater. 16 (2006) 975–979.
[23] W. Wesch, Nucl. Instr. Meth. Phys. Res. B 116 (1996) 305–321.
[24] S.T. Gregg, K.S.W. Sing, Adsorption, Surface Area and Porosity, Academic Press, Salt Laker City, 1997.
[25] P.G. Partridge, Int. Mater. Rev. 26 (1967) 169–194.
[26] D.R. Anderson, Analysis of Silicones, Wiley-Interscience, New York, 1974.
[27] H. Nienhaus, T.U. Kampen, W. Mönch, Surf. Sci. 324 (1995) L328–L332.